Pharmaceutical Sciences and Drug Design
ISSN: 3062-4428
2023, Volume 3, Page No: 256-269

Available online at: www.galaxypub.co/page/journals

Galaxy Publication

Design and Synthesis of Novel 1,2,3-Triazole Derivatives as Non-Steroidal Aromatase Inhibitors for Estrogen-Responsive Breast Cancer

Ahmed Mansour[1]*, Lina Hassan[1], Omar Saeed[1]

[1]Department of Pharmaceutical Chemistry, Faculty of Pharmacy, Cairo University, Cairo, Egypt.

***E-mail** ✉ ahmed.mansour@outlook.com

Received: 29 January 2023; **Revised:** 12 April 2023; **Accepted:** 18 April 2023

ABSTRACT

Aromatase inhibitors (AIs) exhibit promising characteristics as therapeutic agents for estrogen-dependent breast cancer by inhibiting aromatase, the essential enzyme responsible for estrogen biosynthesis. The currently approved AIs for breast cancer therapy by the Food and Drug Administration are associated with significant adverse effects. Therefore, the development of novel AIs with enhanced specificity and potency is crucial. This study describes the synthesis and characterization of new nonsteroidal aromatase inhibitors incorporating triazole moieties, intended for the management of hormone-dependent breast cancer in postmenopausal women. A series of 1,2,3-triazole-based compounds was successfully prepared, and their structures were confirmed using spectral data (FT-IR, ^{13}C NMR, ^{1}H NMR, mass spectrometry) and elemental analysis. The physical properties of these novel derivatives were also documented. The compounds were evaluated for anticancer activity in breast cancer cell lines (MCF7 and T-47D) as well as in a normal breast cell line (MCF 10A), assessing their impact on cell proliferation, migration, and invasion. The findings indicate that these compounds demonstrate promising and selective anticancer effects.

Keywords: 1,2,3-triazoles, Aromatase inhibitors, Breast cancer, Hormone therapy, Gelatin degradation, RNA extraction and real-time qPCR

How to Cite This Article: Mansour A, Hassan L, Saeed O. Design and Synthesis of Novel 1,2,3-Triazole Derivatives as Non-Steroidal Aromatase Inhibitors for Estrogen-Responsive Breast Cancer. Pharm Sci Drug Des. 2023,3:256-69. https://doi.org/10.51847/Flor0cKEu2

Introduction

Breast cancer (BC) impacts approximately 2.5 million women each year and remains the most frequently diagnosed cancer among women. It ranks second only to lung cancer as the primary cause of cancer-related mortality in women across various age groups worldwide. Around 70% of cases involve hormone-responsive BC with elevated expression of estrogen receptors (ERs) [1-3]. Postmenopausal women face an increased risk of developing estrogen-dependent cancer due to estrogen synthesis in peripheral tissues [4, 5]. In these patients, estrogen significantly drives cancer cell proliferation, invasion, and metastasis [6, 7]. Specifically, estrogen contributes to cancer initiation and progression through two mechanisms: (1) functioning as a mitogen [8-11], promoting increased mitosis in breast tissue, which may introduce replication errors leading to mutations and oncogenesis, (2) certain estrogen metabolites acting as carcinogens that directly damage DNA [12-14]. Furthermore, elevated plasma estrogen levels correlate with greater risks of recurrence and metastasis in ER-positive breast cancer patients.

Estrogen biosynthesis occurs through demethylation and aromatization of androgens catalyzed by aromatase (CYP19), the rate-limiting enzyme in this process. Aromatase belongs to the cytochrome P450 family of heme-containing monooxygenases [15, 16]. It forms a microsomal enzyme complex comprising two key components: NADPH-cytochrome P450 reductase (a flavoprotein) and the hemoprotein CYP19.

Two primary approaches exist to control hormone-dependent BC progression: (1) blocking the ER signaling pathway with antagonists or degraders, or (2) suppressing estrogen production via aromatase inhibitors (AIs) [17-

22]. Tamoxifen (TAM), a selective ER modulator, is widely employed in ER-positive BC and reduces recurrence rates by 40–50% while lowering BC-related mortality [16, 23-25]. Nevertheless, resistance to TAM frequently develops in BC cells, and its use is linked to heightened risks of endometrial cancer and hepatic abnormalities [26-28].

AIs generally produce fewer side effects than ER antagonists due to the absence of estrogenic activity on the vasculature and uterus, making them the preferred first-line therapy for postmenopausal women with ER-positive BC [17, 29]. AIs are classified into two categories based on their mode of action. Type 1 includes steroidal AIs, such as exemestane and formestane, which irreversibly inactivate aromatase. Type 2 encompasses nonsteroidal AIs, including letrozole [21, 27, 30, 31], vorozole, and anastrozole, which have received Food and Drug Administration approval [10-12]. The triazole ring forms the central scaffold in nonsteroidal AIs [7-9], where the nitrogen atom coordinates with the heme iron, critically impairing enzyme function.

Overall, nonsteroidal AIs offer several benefits, as they selectively block the final step of estrogen synthesis without affecting other hormones derived from the same pathway. They achieve reversible inhibition of aromatase, and clinical trials comparing them to estrogen receptor modulators (e.g., ATAC trial) have shown superior outcomes with notable therapeutic advantages. However, prolonged use of current nonsteroidal AIs may lead to reproductive issues, osteoporosis, androgenic effects, and arthralgia. Additionally, they partially inhibit cytochromes involved in xenobiotic metabolism (2D6, 2C8/9, 1A1, 1A2, and 3A4), thereby elevating risks of drug–drug interactions.

Thus, there remains a pressing need for novel AIs capable of achieving full estrogen suppression at doses devoid of substantial toxicity or specific adverse effects. In this work, we report the synthesis, chemical, and physical characterization of new triazole-based compounds designed to inhibit aromatase. These newly synthesized molecules were assessed in vitro for anticancer activity, revealing promising properties and potential for further development as anti-breast cancer agents in vivo.

Materials and Methods

Chemistry instrumentation

Melting points of the synthesized compounds were recorded without correction on an electrothermal apparatus. Infrared spectra were obtained on KBr disks using a Shimadzu FT-IR 8101 PC spectrophotometer. Proton and carbon-13 NMR spectra were acquired in DMSO-d_6 on a Bruker 500 MHz spectrometer, with chemical shifts reported in ppm relative to tetramethylsilane as internal standard. Elemental analyses were conducted at the Microanalytical Unit of Cairo University. Mass spectra were recorded on a Shimadzu GC-MS QP1000 EX instrument.

Synthesis

1-(1-(4-Methoxyphenyl)-5-methyl-1H-1,2,3-triazol-4-yl)ethan-1-one (1)

Beige crystals. Yield: 56%, m.p.: 217–219 °C, FT-IR (KBr, cm^{-1}): ν 1680 (C=O), 1612 (C=N), 1590 (C=C), ^{1}H-NMR (DMSO-d_6): δ 2.34 (s, 3H, CH_3), 2.49 (s, 3H, CH_3), 3.73 (s, 3H, OCH_3), 7.03 (d, 2H, 2CH), 7.40 (d, 2H, 2CH) ppm, ^{13}C-NMR (100 MHz, DMSO-d_6): δ 9.57, 27.44 (2 CH_3), 55.58 (OCH_3), 114.75, 126.66, 127.74, 137.66, 142.65, 160.23 (Ar-C), 193.27 (C=O) ppm, MS m/z (%): 231 (M^+, 62). Anal. Calcd. for $C_{12}H_{13}N_3O_2$ (231.26): C, 62.33, H, 5.67, N, 18.17, Found: C, 62.37, H, 5.62, N, 18.14%.

Methyl 2-(1-(1-(4-Methoxyphenyl)-5-methyl-1H-1,2,3-triazol-4-yl)ethylidene)hydrazine-1-carbodithioate (3)

A solution of 1-(1-(4-methoxyphenyl)-5-methyl-1H-1,2,3-triazol-4-yl)ethan-1-one (1) (1.15 g, 5 mmol) and methyl hydrazinecarbodithioate 2 (0.6 g, 5 mmol) in 20 mL ethanol, catalyzed by 1 mL hydrochloric acid, was stirred at ambient temperature for 2 h and monitored by TLC. The precipitated product was filtered, rinsed with water/ethanol mixture, and recrystallized from ethanol to afford yellow crystals. Yield: 82%, m.p.: 175–177 °C, FT-IR (KBr, cm^{-1}): ν 3382 (NH), 1620 (C=N), 1590, ^{1}H-NMR (DMSO-d_6): δ 2.46 (s, 3H, CH_3), 2.50 (s, 3H, CH_3), 2.51 (s, 3H, CH_3), 3.80 (s, 3H, OCH_3), 7.09 (d, 2H, 2CH), 7.48 (d, 2H, 2CH), 12.45 (s, 1H, NH) ppm, ^{13}C-NMR (100 MHz, DMSO-d_6): δ 10.70, 14.83 and 17.12 ($3CH_3$), 55.56 (OCH_3), 114.67, 126.90, 128.24, 133.65, 141.37, 148.19 and 160.05 (Ar-C), 199.63 (C=S) ppm, MS m/z (%): 335 (M^+, 17). Anal. Calcd. for $C_{14}H_{17}N_5OS_2$ (335.44): C, 50.13, H, 5.11, N, 20.88, Found: C, 50.18, H, 5.06, N, 20.82%.

General procedure for synthesis of compounds 4–7

Compound 3 (1.67 g, 5 mmol) was combined with the appropriate hydrazonoyl halide (5 mmol) and 2–3 drops of diisopropylethylamine (DIPEA) in 10 mL ethanol. The mixture was stirred at room temperature for 2 h, then continued for about 5 h total, with progress tracked by TLC. The resulting solid was isolated, washed with water/ethanol, and recrystallized from a suitable solvent to yield compounds 4–7.

*1-(5-((1-(1-(4-Methoxyphenyl)-5-methyl-1H-1,2,3-triazol-4-yl)ethylidene)hydrazono)-4-phenyl-4,5-dihydro-1,3,4-thiadiazol-2-yl)ethan-1-one (4***)**

Yellow crystals. Yield: 76%, m.p.: 264–266 °C, FT-IR (KBr, cm^{-1}): ν 1685 (C=O), 1620 (C=N), 1585, ^{1}H-NMR (DMSO-d_6): δ 2.60 (s, 3H, CH_3), 2.63 (s, 3H, CH_3), 2.73 (s, 3H, CH_3), 3.89 (s, 3H, OCH_3), 7.05–8.12 (m, 9H, ArH) ppm, ^{13}C-NMR (100 MHz, DMSO-d_6): δ 11.78, 16.11, 25.15 (3 CH_3), 55.72 (s, 3H, OCH_3), 114.77, 115.49, 121.19, 126.89, 128.99, 129.57, 133.78, 139.44, 142.75, 150.46, 158.05, 160.59, 164.55 (Ar-C), 189.98 (C=O) ppm, MS m/z (%): 447 (M^+, 25). Anal. Calcd. for $C_{22}H_{21}N_7O_2S$ (447.52): C, 59.05, H, 4.73, N, 21.91, Found: C, 59.09, H, 4.68, N, 21.85%.

1-(5-((1-(1-(4-Methoxyphenyl)-5-methyl-1H-1,2,3-triazol-4-yl)ethylidene)hydrazono)-4-(p-tolyl)-4,5-dihydro-1,3,4-thiadiazol-2-yl)ethan-1-one (5)

Yellow crystals. Yield: 89%, m.p.: 239–241 °C, FT-IR (KBr, cm^{-1}): ν 1680 (C=O), 1622 (C=N), 1600 (C=C), ^{1}H-NMR (DMSO-d_6): δ 2.42 (s, 3H, CH_3), 2.59 (s, 3H, CH_3), 2.62 (s, 3H, CH_3), 2.68 (s, 3H, CH_3), 3.89 (s, 3H, OCH_3), 7.05–7.96 (m, 8H, Ar-H) ppm, ^{13}C-NMR (100 MHz, DMSO-d_6): δ 11.79, 16.05, 21.14, 25.13 (4 CH_3), 55.72 (OCH_3), 114.77, 115.44, 122.05, 126.86, 129.60, 130.04, 133.73, 137.07, 142.82, 150.36, 157.76, 160.59, 164.70 (Ar-C), 189.99 (C=O) ppm, MS m/z (%): 461 (M^+, 58). Anal. Calcd. for $C_{23}H_{23}N_7O_2S$ (461.54): C, 59.85, H, 5.02, N, 21.24, Found: C, 59.82, H, 4.98, N, 21.19%.

Ethyl 5-((1-(1-(4-Methoxyphenyl)-5-methyl-1H-1,2,3-triazol-4-yl)ethylidene)hydrazono)-4-phenyl-4,5-dihydro-1,3,4-thiadiazole-2-carboxylate (6)

Yellowish white crystals. Yield: 86%, m.p.: 215–217 °C, FT-IR (KBr, cm^{-1}): ν 1725 (C=O, ester), 1620 (C=N), 1600 (C=C), ^{1}H-NMR (DMSO-d_6): δ 1.40 (s, 3H, $COOCH_2CH_3$), 2.60 (s, 3H, CH_3), 2.69 (s, 3H, CH_3), 3.89 (s, 3H, OCH_3), 4.43 (q, 2H, $COOCH_2CH_3$), 7.05–8.10 (m, 9H, ArH) ppm, ^{13}C-NMR (100 MHz, DMSO-d_6): δ 11.77, 14.27 (2CH_3), 55.73 (OCH_3), 63.02 (CH_2), 114.76, 122.13, 126.91, 126.99, 128.95, 133.62, 139.41, 142.63, 142.38, 157.79, 159.01, 160.57, 164.29 (Ar-C), 160.57 (C=O), 164.29 (C=N) ppm, MS m/z (%): 477 (M^+, 12). Anal. Calcd. for $C_{23}H_{23}N_7O_3S$ (477.54): C, 57.85, H, 4.85, N, 20.53, Found: C, 57.89, H, 4.82, N, 20.51%.

Ethyl 5-((1-(1-(4-Methoxyphenyl)-5-methyl-1H-1,2,3-triazol-4-yl)ethylidene)hydrazono)-4-(p-tolyl)-4,5-dihydro-1,3,4-thiadiazole-2-carboxylate (7)

Orange crystals. Yield: 92%, m.p.: 210–212 °C, FT-IR (KBr, cm^{-1}): ν 1715 (C=O, ester), 1610 (C=N), 1590 (C=C), ^{1}H-NMR ($CDCl_3$-d_6): δ 1.40 (s, 3H, $COOCH_2CH_3$), 2.40 (s, 3H, CH_3), 2.60 (s, 3H, CH_3), 2.68 (s, 3H, CH_3), 3.89 (s, 3H, OCH_3), 4.42 (s, 2H, $COOCH_2CH_3$), 7.05 (d, 2H, J = 5 Hz), 7.25 (d, 2H, J = 10 Hz), 7.38 (d, 2H, J = 10 Hz), 7.93 (d, 2H, J = 5 Hz) ppm, ^{13}C-NMR (100 MHz, DMSO-d_6): δ 11.76, 14.27, 16.07 (3CH_3) 55.72 (OCH_3), 62.96 (CH_2), 112.75, 114.82, 122.19, 126.65, 128.71, 129.11, 133.63, 136.99, 138.57, 142.31, 157.08, 158.65 (Ar-H), 160.74 (C=O), 164.47 (C=N) ppm, MS m/z (%): 491 (M^+, 45). Anal. Calcd. for $C_{24}H_{25}N_7O_3S$ (491.17): C, 58.64, H, 5.13, N, 19.95, Found: C, 58.68, H, 5.09, N, 19.91%.

Computational study

The crystallographic coordinates of human aromatase were obtained from the Protein Data Bank (www.rcsb.org) [32], accession code 4GL7. All water molecules and the bound ligand were deleted, and the resulting protein structure was exported as a PDB file in Biovia Discovery Studio 2021 to prepare it for docking. Active site detection and docking calculations were conducted using the CB-Dock online platform (<http://clab.labshare.cn/cb-dock/php/>) under default parameters. Docking of the seven compounds into 4GL7 targeted a cavity of volume 379, centered at x: 85.07, y: 50.88, z: 50.19 with grid dimensions of 27 × 27 × 27.

Aromatase enzymatic activity assay

Inhibition of aromatase was quantified with a commercial fluorogenic kit (Abcam) according to the supplier's guidelines. Reactions were run in the presence of DMSO alone or with compound concentrations rising from 0 to 100 µM. A parallel set included 1 µM letrozole as positive control. Fluorescence was monitored every 50 s during a 1 h incubation at 37 °C. Half-maximal inhibitory concentrations (IC_{50}) were computed in GraphPad Prism 9.0 (GraphPad Software).

Cell culture

Cell lines MCF 10A, MCF7, and T-47D were purchased from ATCC (Manassas, VA, USA). Non-malignant MCF 10A cells were propagated in DMEM/F12 medium fortified with 5% horse serum, 2 mM L-glutamine, 20 ng/mL EGF, 10 µg/mL insulin, 0.5 mg/mL hydrocortisone, and 100 ng/mL cholera toxin. MCF7 cells were maintained in DMEM with 10% FBS and 2 mM L-glutamine. T-47D cells were cultured in RPMI medium supplemented with 10% FBS and 2 mM L-glutamine. Cultures were kept at 37 °C in a humidified 5% CO_2 environment.

Anticancer assay

MTT assay

For viability testing, MCF 10A cells were dispensed into 96-well plates at 8000 cells/well (24 h assay), 7000 cells/well (48 h), or 6000 cells/well (72 h) in 200 µL medium, with triplicates per condition. Cancer lines MCF7 and T-47D were plated at 10,000 cells/well (24 h), 8000 cells/well (48 h), or 7000 cells/well (72 h). After 24 h adhesion, medium was refreshed with vehicle or compound doses spanning 0–100 µM (compounds 4, 5, 6, and 7). Incubation proceeded for the designated durations at 37 °C. Then, 20 µL MTT (5 mg/mL) was added per well for a further 2 h incubation. Supernatant was aspirated, formazan dissolved in DMSO, and absorbance recorded at 470 nm on a Cytation 3 reader (BioTek, Winooski, VT, USA). Viability percentages were derived relative to DMSO controls. Differences were analyzed by Student's t-test, and IC_{50} values determined using GraphPad Prism 9.0 (GraphPad Software, Inc., La Jolla, CA, USA).

RNA extraction and real time qPCR

Cells (MCF 10A, MCF7, T-47D) were seeded at 280,000 cells/well in 6-well plates. Following overnight settlement, cultures received 1 µM of compounds 4, 5, 6 or 7 for 24 h. Total RNA was purified with RNeasy kits (Qiagen, Hilden, Germany), and cDNA synthesized via QuantiTect reverse transcription kits (Qiagen). Amplification employed LightCycler® 480 SYBR Green I Master on a LightCycler 480 II system (Roche, Indianapolis, IN, USA). Cycling conditions started with 15 min at 95 °C, then 40 cycles of 10 s at 95 °C, 30 s at 60 °C, and 30 s at 72 °C. Normalization used GAPDH as internal control. Relative expression changes versus DMSO-treated samples were calculated, with significance tested by Student's t-test.

Wound healing assay

MCF 10A, MCF7, and T-47D cells were seeded in 12-well plates at 600,000 cells per well. After 24 h, the monolayers reached full confluence. A linear scratch was then created across each well using a 10 µL pipette tip, after which cells were maintained overnight with 1 µM of 4, 5, 6 or 7 in medium containing 0.5% FBS. Wound images were captured at 0 h (right after scratching) and following 24 h of compound exposure, employing an inverted Zeiss Axio Observer Z1 widefield microscope fitted with an AxioCam MRm grayscale CCD camera and operated via ZEN pro software (Zeiss, Oberkochen, Germany, <https://www.bioz.com/result/zen%20pro%20software/product/Carl%20Zeiss>). Wound areas were measured with ImageJ software (National Institutes of Health, Bethesda, MD, USA, <https://imagej.net/ij/>, 1997–2018), and percentage wound closure was determined according to the equation:

$$\%\mathrm{WoundClosure} = \left(\frac{\mathrm{A1} - \mathrm{A2}}{\mathrm{A1}}\right) \times 100 \quad (1)$$

In the formula, A1 denotes the initial wound area (at t=0), whereas A2 indicates the area remaining after 24 h. Furthermore, wound closure percentages for treated samples were expressed as fold differences relative to the baseline closure observed in DMSO-only controls. Statistical evaluation employed Student's t-test.

Gelatin degradation (invasion) assay

Coverslips pre-coated with fluorescent gelatin were generated following an established procedure [33]. Cells were inoculated onto these substrates in 24-well plates at 70,000 cells/well. After an initial 24 h incubation for attachment, samples received 1 μM of compounds 4, 5, 6 or 7, followed by fixation 24 h later in 4% paraformaldehyde (v/v) for 15 min at ambient temperature. Cytoskeletal F-actin and cell nuclei were then visualized by staining with Alexa Fluor™ 488 Phalloidin (Invitrogen, Carlsbad, CA, USA) and Hoechst 33342 (Invitrogen, Carlsbad, CA, USA), respectively. Confocal microscopy was performed on an LSM 510 system (Zeiss, Oberkochen, Germany), with degraded regions quantified via ImageJ software. Differences were tested for significance using Student's t-test.

Results and Discussion

Chemical synthesis and characterization of compounds 1, 3, 4, 5, 6, and 7

Fine-tuning the connecting units between diverse bioactive heterocyclic systems and 1,2,3-triazole rings is viewed as an effective approach to improve their potential in anticancer therapy. Toward this goal, 1-azido-4-methoxybenzene was reacted with pentane-2,4-dione in a base-catalyzed condensation, employing sodium ethoxide in refluxing ethanol, to produce 1-(1-(4-methoxyphenyl)-5-methyl-1H-1,2,3-triazol-4-yl)ethan-1-one (1). The identity of this acetyl-substituted triazole 1 was established through comprehensive spectral analysis and elemental composition data. In its FT-IR spectrum, a prominent band appeared at 1680 cm^{-1}, indicative of the carbonyl stretch. The ^{1}H NMR spectrum featured singlet peaks at 2.34 and 2.49 ppm for the methyl protons, together with another singlet at 3.73 ppm assigned to the methoxy group. The aromatic region displayed two doublets at δ 7.03 and 7.40 ppm (J = 10 Hz). The ^{13}C NMR spectrum included diagnostic peaks at 9.57 and 27.44 ppm for the methyl carbons, 55.58 ppm for the methoxy carbon, and 193.27 ppm for the carbonyl carbon. Mass spectrometry revealed a molecular ion at m/z = 231 (M^{+}, 18%), in agreement with the formula $C_{12}H_{13}N_3O_2$. Additional confirmation of compound 1 came from its use as a central building block in further heterocycle construction bearing the 1,2,3-triazole core. It was treated with methyl hydrazinecarbodithioate 2, leading to methyl 2-(1-(1-(4-methoxyphenyl)-5-methyl-1H-1,2,3-triazol-4-yl)ethylidene)hydrazine-1-carbodithioate (3). Structural elucidation of 3 relied on spectroscopic evidence. Its FT-IR spectrum showed intense bands at 3337 cm^{-1} (NH) and 1687 cm^{-1} (C=O). In the ^{1}H NMR, methyl proton signals emerged at 2.45, 2.50, and 2.51 ppm, while the methoxy protons resonated at 3.80 ppm. Aromatic doublets were observed at 7.09 and 7.48 ppm (J = 10.0 Hz), and a broad singlet at 12.45 ppm corresponded to the NH. The ^{13}C NMR displayed methyl carbon peaks at 10.70, 14.83, and 17.12 ppm, a methoxy signal at 55.56 ppm, a thiocarbonyl at 199.63 ppm, and aromatic carbons at 114.67, 126.90, 128.24, 133.65, 141.37, 148.19, and 160.05 ppm. Compound 3 then served as a precursor for generating novel hybrid molecules combining 1,3,4-thiadiazole and 1,2,3-triazole moieties. Cyclization with suitable hydrazonoyl halides yielded the targeted derivatives 4–7, as outlined in **Scheme 1.**

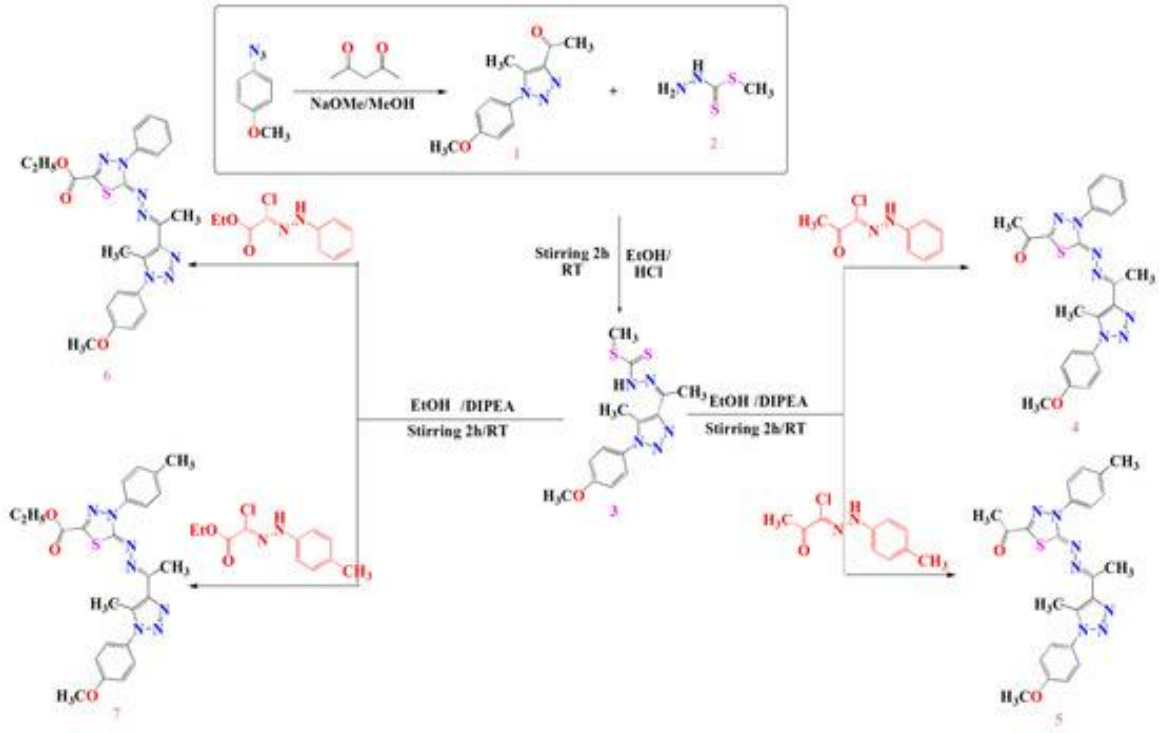

Scheme 1. Synthetic routes leading to compounds 3, 4, 5, 6, and 7.

The molecular structures of the thiadiazole-containing compounds 4–7 were verified through detailed spectral interpretation. For compound 4, the ^{1}H NMR spectrum presented methyl signals at 2.60, 2.63, and 2.73 ppm, a methoxy singlet at 3.89 ppm, and aromatic protons as a multiplet between 7.05 and 8.12 ppm. Corresponding ^{13}C NMR data included methyl carbons at 11.78, 16.11, and 25.15 ppm, methoxy at 55.72 ppm, carbonyl at 189.98 ppm, and aromatic carbons spanning 114.77 to 164.55 ppm. In a similar manner, compound 5 exhibited ^{1}H NMR methyl peaks at 2.42, 2.59, 2.62, and 2.68 ppm, methoxy at 3.89 ppm, and aromatic multiplet from 7.05 to 7.96 ppm. Its ^{13}C NMR showed methyl signals at 11.79, 16.05, 21.14, and 25.13 ppm, methoxy at 55.72 ppm, carbonyl at 189.99 ppm, and aromatic carbons from 114.77 to 164.70 ppm. For compound 6, the ^{1}H NMR revealed an ethyl triplet at 1.40 ppm (CH_3 of ester), methyl singlets at 2.60 and 2.69 ppm, methoxy singlet at 3.89 ppm, ethyl quartet at 4.43 ppm (CH_2 of ester), and aromatic multiplet from 7.05 to 8.10 ppm. The ^{13}C NMR indicated methyl carbons at 11.77 and 14.27 ppm, methoxy at 55.73 ppm, methylene at 63.02 ppm, ester carbonyl at 160.57 ppm, C=N at 164.29 ppm, and aromatic carbons between 114.76 and 159.01 ppm. Compound 7 displayed comparable ^{1}H NMR features: ethyl triplet at 1.40 ppm, methyl singlets at 2.60 and 2.68 ppm, methoxy at 3.89 ppm, ethyl quartet at 4.42 ppm, and aromatic doublets at 7.05, 7.25, 7.38, and 7.93 ppm. Its ^{13}C NMR featured methyl signals at 11.76 and 14.27 ppm, methoxy at 55.72 ppm, methylene at 62.96 ppm, ester carbonyl at 160.74 ppm, C=N at 164.47 ppm, and aromatic carbons from 112.75 to 158.65 ppm (see Supporting Information).

Computational study

Docking simulations revealed binding energies of −6.9, −7.0, −9.6, −10.1, −9.7, and −9.8 kcal/mol for compounds 1, 3, 4, 5, 6, and 7, respectively. As presented in **Table 1 and Figure 1,** compounds 1 and 3 fitted into the aromatase binding site, each forming a pair of hydrogen bonds. These contacts, however, occurred with residues Ala438 and Gly439, which are less optimal compared to the interactions of the co-crystallized inhibitor with Arg115 and Met374. The reference inhibitor **(Figure 2)** uses these two key hydrogen bonds to achieve ideal alignment, allowing it to occupy the hydrophobic cavity effectively and seal the substrate access pathway flanked by Ser478 and Thr310. By contrast, compounds 1 and 3 showed altered positioning and distinct hydrogen bonding. In comparison **(Figures 1 and 2),** compounds 4, 5, 6, and 7 replicated the critical hydrogen bonds with Arg115 and Met374 seen in the co-crystallized ligand, positioning them favorably to impede substrate entry. Particularly for compound 7 **(Figure 1),** multiple additional contacts were observed, promoting strong anchorage in the active site. Furthermore, it formed a C–H interaction with the gatekeeper residue Thr310, thereby obstructing the narrow entrance between Ser478 and Thr310 and achieving effective enzyme inhibition. The co-crystallized inhibitor

similarly restricts substrate access via its bonds with Arg115 and Met374, whereas compounds 1 and 3 lack this precise arrangement. Compounds 4, 5, 6, and 7, however, mirrored the native inhibitor's bonding pattern **(Figures 1 and 2)** and demonstrated comparable blocking potential. Compound 7 distinguished itself with abundant stabilizing contacts and a strategic C–H bond to Thr310, preventing substrate passage through the Ser478–Thr310 channel and delivering robust aromatase inhibition.

a)

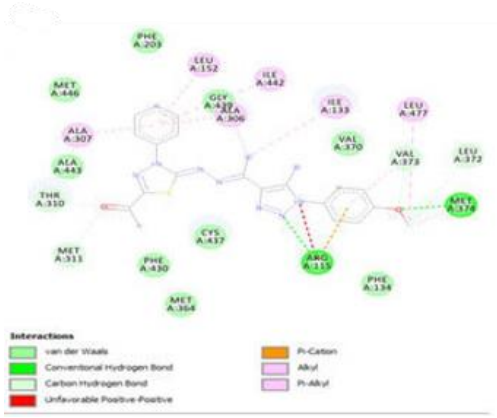

b)

Compound 4

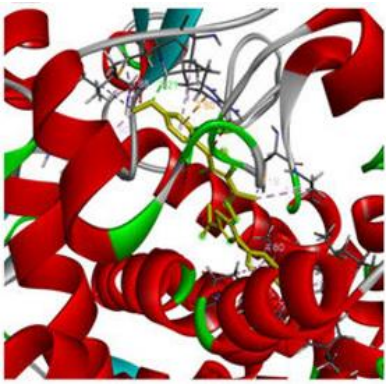

a)

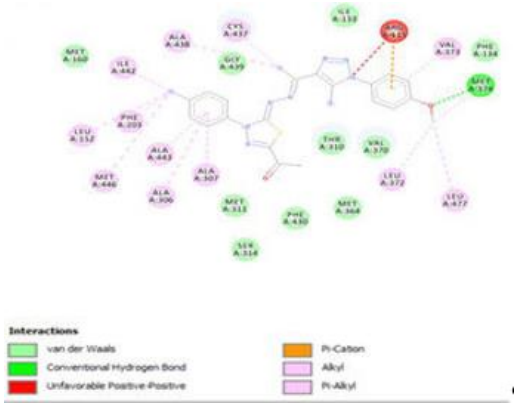

b)

Compound 5

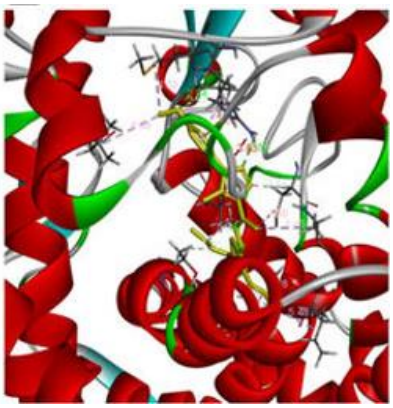

a)

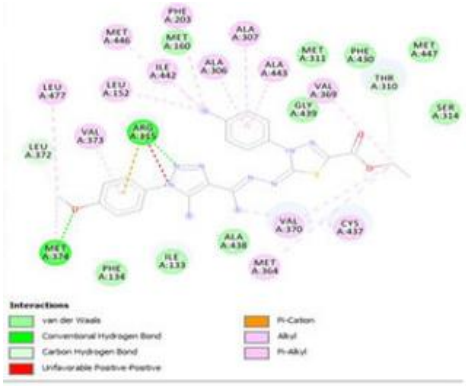

b)

Compound 6

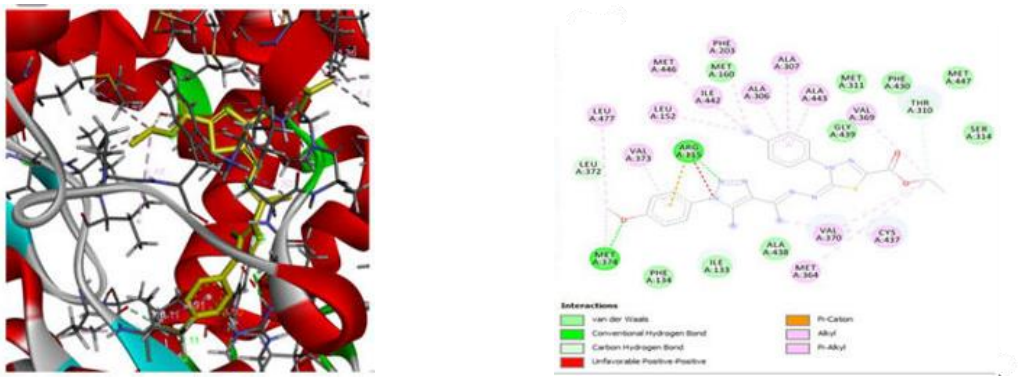

a) b)

Compound 7

Figure 1. Docking poses for the prepared compounds 4, 5, 6, and 7 in the human aromatase enzyme active site. (a) 3D and (b) 2D views of the complexes. Hydrogen bonds appear as blue/green dashed lines, π-stacking as orange lines.

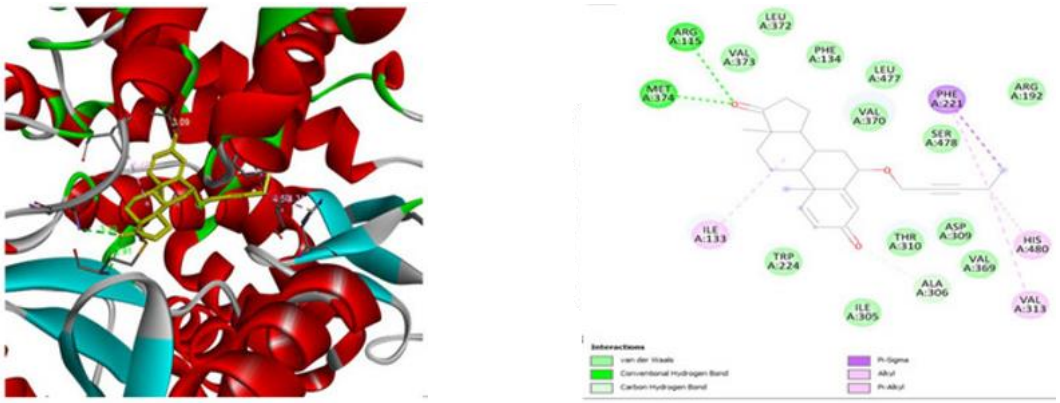

a) b)

co-crystallized inhibitor

Figure 2. Interactions of the co-crystallized inhibitor in the human aromatase enzyme. (a) 3D and (b) 2D views of the complex. Hydrogen bonds appear as blue/green dashed lines, π-stacking as orange lines.

Table 1. Docking scores for synthesized compounds 1 (C1), 3 (C3), 4 (C4), 5 (C5), 6 (C6), and 7 (C7) alongside the co-crystallized ligand.

Compound	Binding Energy (kcal/mol)	Hydrogen Bonds	Hydrophobic/Residual Interactions
C1	-6.9	(2): Gly439-Ala438	Leu152-Ala307-Met446-Ala306, Phe203-Ile442
C3	-7.0	Gly439-Ala438	Leu152-Ala307-Met446-Ala306-Phe203-Ile442-Ile132-Cys437-Val373
C4	-9.6	(2): Arg115-Met374	Leu152-Ala307-Ala306-Leu372-Leu377-Arg115-Ile133-Ile442-Met311
C5	-10.1	(1): Met374	Leu152-Ala307-Met446-Ala306-Phe203-Ile442-Arg115-Leu372-Leu377-Ala343-Val373-Cys437-Ala438
C6	-9.7	(2): Arg115-Met374	Ala307-Ala306-Ala343-Met364-Cys437-Leu477-Ala438-Arg115-Val373-Ile442
C7	-9.8	(2): Arg115-Met374	Leu152-Ala307-Met446-Leu372-Leu377-Leu372-Leu377-Thr310-Cys437-Val370-Met364-Val370-Ala443

(6α,8α)-6-(pent-2-yn-1-yloxy)androsta-1,4-diene-3,17-dione (Inhibitor)	-11.1	(2): Arg115-Met374	Phe220-His480-Val313-Ile133-Ala306

Overall, the modeling data highlighted stronger binding scores and engagement with essential residues for compounds 4, 5, 6, and 7 within the aromatase site, justifying their progression to in vitro anticancer activity screening.

In vitro evaluation of aromatase inhibition by compounds 4, 5, 6, and 7

Prompted by promising docking predictions, compounds 4, 5, 6, and 7 underwent in vitro testing to measure their aromatase inhibitory potency through determination of IC_{50} values. Activity was monitored using a fluorometric assay (see materials and methods section) over a compound concentration gradient from 0 to 100 μM **(Figure 3a).** The recorded IC_{50} values were 3.62 μM for compound 4, 1.991 μM for compound 5, 3.57 μM for compound 6, and 2.993 μM for compound 7. These experimental results correlated well with computational findings, confirming compound 5 as the lead inhibitor across both platforms. **Figure 3b** depicts the temporal inhibition profile at 1 μM concentration over 60 minutes for all four compounds. Their efficacy was evaluated relative to letrozole, a standard non-steroidal aromatase inhibitor in clinical use. Each compound achieved roughly 50% reduction in enzyme activity under these conditions.

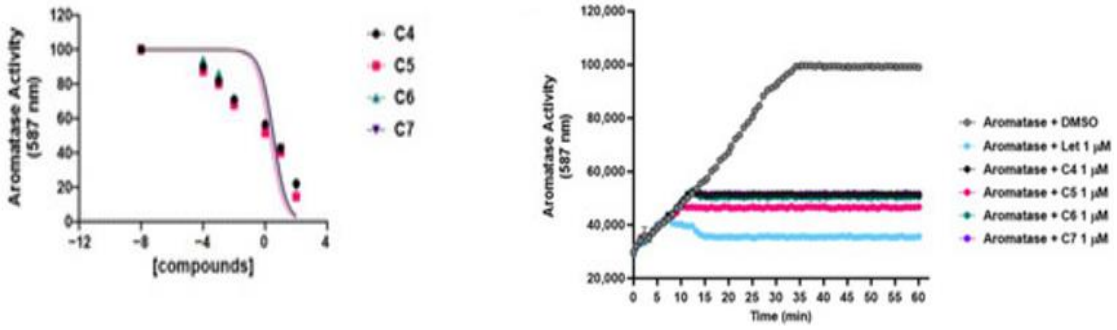

a) b)

Figure 3. In vitro aromatase inhibition profiles for compounds 4, 5, 6, and 7. (a) Enzyme activity assessed without or with escalating doses (0–100 μM) of compounds 4 (C4), 5 (C5), 6 (C6), and 7 (C7) via fluorometric assay (see materials and methods section). Dose–response curves display log_{10} compound concentrations for C4 (black circles), C5 (pink squares), C6 (green triangles), and C7 (purple triangles) plotted against normalized fluorescence (587 nm). Calculated IC_{50} values are detailed in results and discussion section. Values represent mean ± SD from triplicate experiments. (b) Time-course monitoring of aromatase activity (DMSO control) or with 1 μM letrozole (Let) or compounds 4 (C4), 5 (C5), 6 (C6), and 7 (C7) up to 60 minutes. Values represent mean ± SD from triplicate experiments.

Anticancer assays

The antitumor potential of compounds 4, 5, 6, and 7 was investigated through assessments of breast cancer (BC) cell proliferation, migration, and invasive capacity.

Progression of estrogen receptor-positive BC is closely tied to circulating estrogen levels and local aromatase-driven estrogen production. To determine how 4, 5, 6, and 7 influence BC cell growth, the aromatase-overexpressing cell lines MCF7 and T-47D were employed, as their proliferation depends on aromatase activity. Cells received graded doses of the compounds (0–100 μM) over 24, 48, and 72 h periods, followed by viability measurement using MTT assay. Exposure produced clear dose- and duration-dependent declines in viability. Corresponding IC_{50} values for each combination of cell line, compound, and duration are listed in **Tables 2 and 3**. On the basis of these data, subsequent mechanistic studies utilized 1 μM concentrations of 4, 5, 6, and 7 applied for 24 h. **Figure 4** displays viability outcomes for MCF7 **(Figure 4a)** and T-47D **(Figure 4b**) cells after 24 h at this dose, revealing roughly 25–30% suppression of proliferation across the series. For selectivity evaluation, healthy breast epithelial cells (MCF 10A) underwent identical exposure, with MTT results showing negligible impact on their growth.

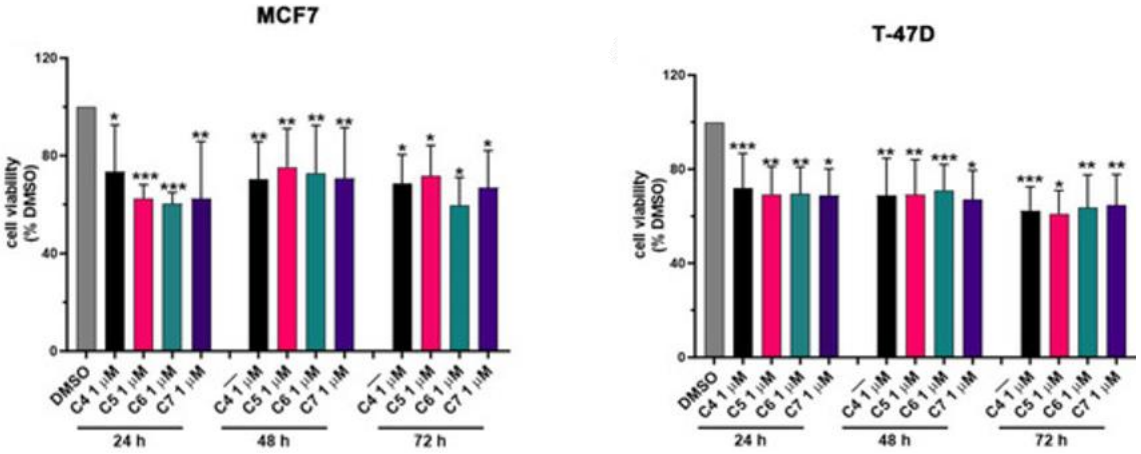

a) b)

Figure 4. Influence of compounds 4, 5, 6, and 7 on MCF7 and T-47D cell growth. Viability was determined via MTT assay in MCF7 (a) and T-47D (b) cells left untreated (DMSO) or exposed to 1 µM of compounds 4 (C4), 5 (C5), 6 (C6), and 7 (C7) for 24, 48, and 72 h. Results are mean ± SD from six replicates. $p < 0.05$, $p < 0.01$, $p < 0.005$ versus DMSO (Student's t-tests).

Table 2. IC_{50} values of 4, 5, 6, and 7 in MCF7 cells.

Compound	24 h	48 h	72 h
C4	3.722 µM	2.267 µM	1.072 µM
C5	3.255 µM	1.201 µM	1.228 µM
C6	3.086 µM	1.417 µM	1.501 µM
C7	2.692 µM	1.052 µM	1.22 µM

Table 3. IC_{50} values of 4, 5, 6, and 7 in T-47D cells.

Compound	24 h	48 h	72 h
C4	3.177 µM	1.685 µM	1.67µM
C5	3.119 µM	1.897 µM	1.5 µM
C6	3.066 µM	1.643 µM	1.1 µM
C7	1.854 µM	1.455 µM	1.317 µM

These data demonstrate that compounds C4, C5, C6, and C7 selectively block aromatase-driven proliferation in breast cancer (BC) cells without exerting substantial influence on the growth of non-malignant breast cells.

To gain deeper insight into how these four aromatase inhibitors (AIs) interfere with the proliferation of cancerous cells, we analyzed the mRNA levels of key genes implicated in cell cycle control and programmed cell death in both treated and untreated cells. The assessment included Cyclin D1, a cell cycle regulator responsive to mitogenic signals that is commonly upregulated in estrogen receptor (ER)-positive BC, where it critically drives tumor development and advancement [34], notably, increased Cyclin D1 levels have also been correlated with poorer survival outcomes among patients with ER-positive BC [34]. We further evaluated c-myc expression upon exposure to C4, C5, C6, and C7, considering the well-documented role of this transcription factor in orchestrating multiple genes linked to BC initiation and evolution, as well as its association with acquired resistance to aromatase inhibitors in BC [22]. Levels of Bax (pro-apoptotic) and Bcl-2 (anti-apoptotic) were likewise monitored, given their established contributions to BC pathogenesis [35]. Experiments involved BC lines (MCF7 and T-47D) alongside a non-cancerous breast line (MCF 10A). Following a 24-hour incubation with 1 µM of each compound, transcriptional activity was measured via real-time qPCR. In non-malignant breast cells, none of the compounds altered the transcription of these target genes. By contrast, in the cancerous lines, all four agents successfully altered expression of the investigated genes. Consistent with predictions, genes favoring cell proliferation (Cyclin D1, c-myc, and Bcl-2) displayed reduced transcription after compound exposure **(Figures 5a–5c)**, whereas transcription of the apoptosis-promoting Bax gene was increased by all four **tr**eatments **(Figure 5d).**

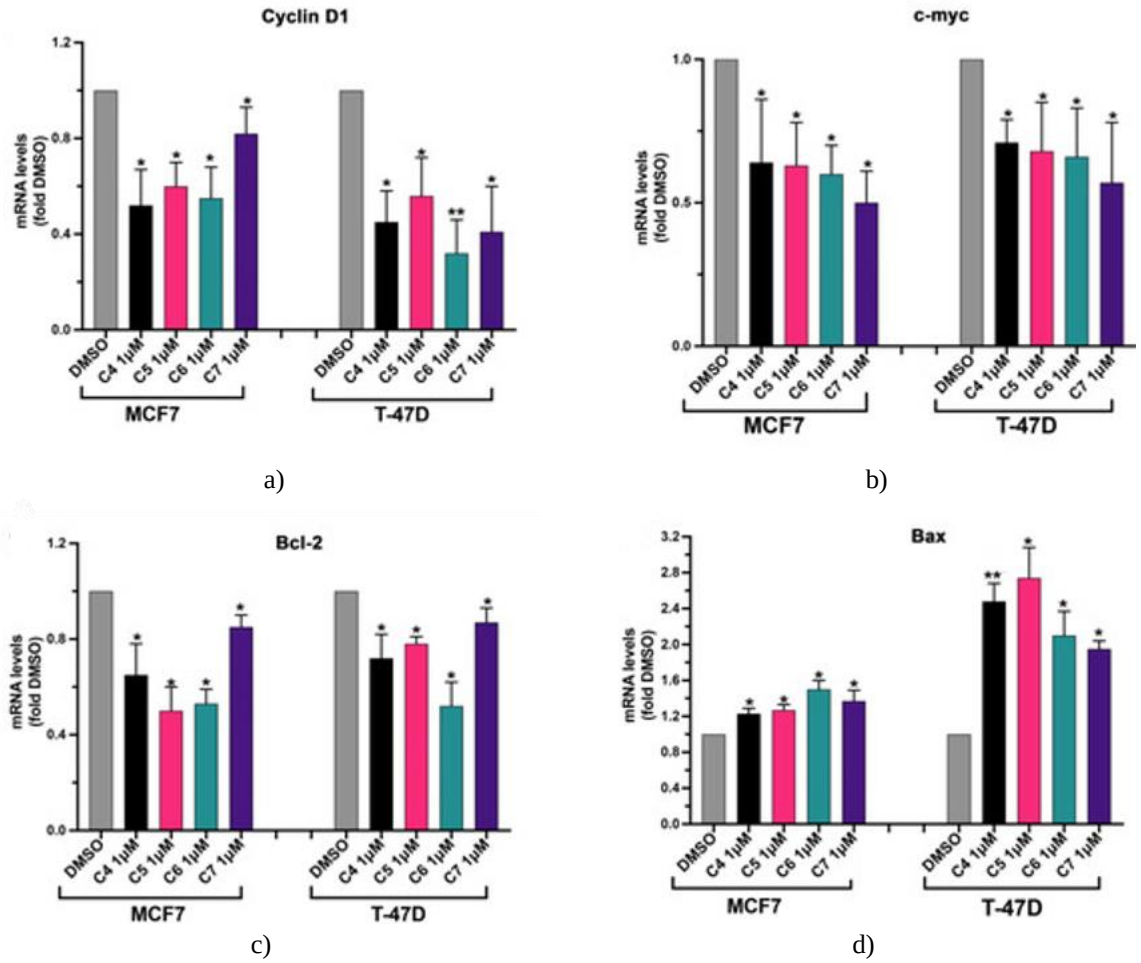

Figure 5. Modulation of proliferation- and apoptosis-related gene expression by compounds 4, 5, 6, and 7 in MCF7 and T-47D cells. Cells were cultured per materials and methods section protocols and exposed to DMSO or 1 μM compounds 4 (C4), 5 (C5), 6 (C6), and 7 (C7) for 24 h. Transcript levels of Cyclin D1 (a), c-myc (b), Bcl-2 (c), and Bax (d) were measured by real-time qPCR, with normalization to GAPDH. Results are mean ± SD from three replicates. $p < 0.05$, $p < 0.01$ versus DMSO (Student's t-tests).

In summary, the tested compounds effectively curb aromatase-reliant BC cell expansion by altering the expression of critical genes governing proliferation and cell survival.

Compounds 4, 5, 6 and 7 inhibit cancer cell migration and invasiveness

Metastasis to distant organs remains the primary cause of mortality in breast cancer (BC) patients [36]. The initial phase of metastasis involves epithelial–mesenchymal transition, a process that endows tumor cells with increased motility and the capacity to break down the extracellular matrix [37]. Estrogen signaling actively promotes metastasis in BC by triggering pathways that facilitate tumor dissemination, colonization, and growth at secondary sites [38]. We evaluated the capacity of 4, 5, 6 and 7 to suppress aromatase-dependent migration and matrix degradation in BC cells.

To assess migratory potential, MCF 10A, MCF7, and T-47D cells were cultured in 96-well plates until full confluence, after which a scratch wound was created as outlined in materials and methods section. Cells were then exposed to 1 μM of 4, 5, 6 and 7 for 24 h in medium containing 0.5% FBS to minimize proliferative contributions to wound closure. Migration was quantified as the percentage of wound closure relative to vehicle-treated cells (DMSO). The compounds exerted no influence on the migration of non-malignant MCF 10A cells. In contrast, they markedly impaired BC cell migration. Specifically, wound closure in MCF7 cells was reduced by approximately 70% with 4 and 5, by about 30% with 6, and by about 40% with 7 **(Figure 6a).** For T-47D cells, migration was diminished by roughly 20% with 4, 6 and 7, and by about 40% with 5 **(Figure 6a).**

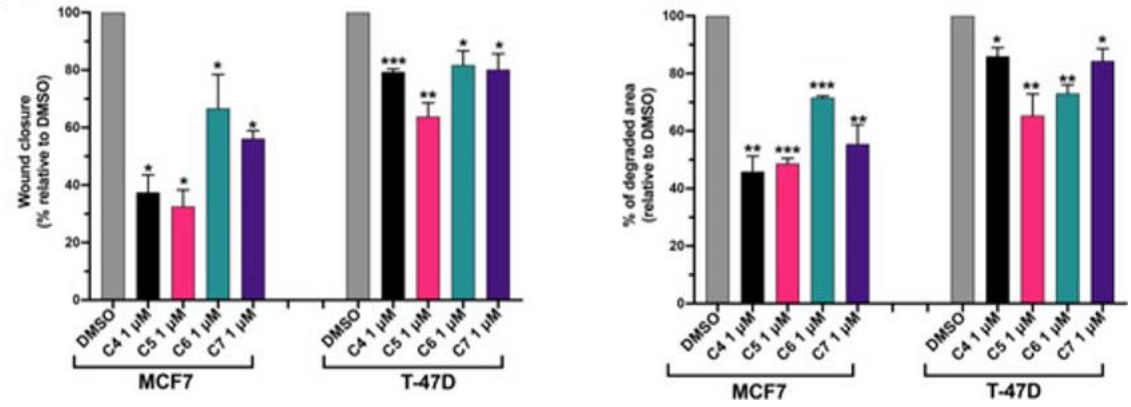

a) b)

Figure 6. Compounds 4, 5, 6 and 7 suppress breast cancer cell migration and invasive properties. (a) MCF7 and T-47D cells were seeded according to materials and methods section. Following wound creation, cells received DMSO or 1 µM of compounds 4 (C4), 5 (C5), 6 (C6) and 7 (C7) for 24 h in medium with 0.5% FBS. Wound closure percentage was determined relative to DMSO controls. Results are mean ± SD from three independent experiments. $p < 0.05$, $p < 0.01$, $p < 0.005$ vs. DMSO (paired Student's t-tests). (b) MCF7 and T-47D cells were prepared as detailed in materials and methods section and treated with DMSO or 1 µM of compounds 4 (C4), 5 (C5), 6 (C6) and 7 (C7) for 24 h. Degraded area was quantified relative to DMSO controls. Results are mean ± SD from three independent experiments. $p < 0.05$, $p < 0.01$, $p < 0.005$ vs. DMSO (paired Student's t-tests).

The impact on extracellular matrix degradation was examined using fluorescent gelatin degradation assays, where gelatin serves as a surrogate for the matrix that tumor cells must proteolyze during invasion. MCF 10A, MCF7, and T-47D cells were grown on fluorescent gelatin-coated coverslips per materials and methods section, then treated with 1 µM of 4, 5, 6 and 7 for 24 h. Degraded area was expressed as a percentage relative to DMSO-treated cells. No alterations in degradation activity were observed in MCF 10A cells, which exhibited inherently lower baseline activity than BC lines. Conversely, in MCF7 cells, 4, 5 and 7 decreased gelatin degradation by around 50%, while 6 achieved approximately 30% reduction **(Figure 6b).** In T-47D cells, matrix degradation was also impaired: 4 and 7 by about 20%, 5 by roughly 35%, and 6 by approximately 25% **(Figure 6b).**
Overall, these findings demonstrate that the evaluated compounds effectively hinder key migratory and matrix-degrading capabilities of BC cells, processes essential for metastatic spread.

Conclusion

Breast cancer continues to pose a significant worldwide public health burden, ranking as one of the primary contributors to cancer-associated fatalities globally. Within its various subtypes, estrogen receptor-positive disease predominates among postmenopausal females [1-3]. Notwithstanding advances in investigative efforts and emerging therapeutic options, the demand persists for more targeted and potent interventions against this condition. Currently, non-steroidal aromatase inhibitors represent standard first-line management for estrogen-dependent breast cancer in this patient group, yielding substantial clinical benefits [39]. Yet, their use is often limited by adverse reactions, notably bone density loss and cardiovascular risks [39]. This has spurred ongoing development of alternative agents capable of targeting aromatase with enhanced tolerability and minimized complications. The current study details the design, preparation, and thorough structural verification of four novel non-steroidal aromatase inhibitors, validated by spectroscopic techniques and elemental composition analysis. Docking simulations illustrated effective engagement of these agents with the enzyme's catalytic pocket, disrupting its function. These computational predictions were corroborated experimentally, as the agents potently curtailed aromatase-reliant growth, motility, and invasive behavior in cultured breast tumor cells. Crucially, selectivity was evident, with negligible influence on non-tumorigenic mammary epithelial cells. Thus, this investigation presents four attractive lead structures for potential breast cancer therapeutics. Planned follow-up studies will assess their efficacy in relevant in vivo tumor models.

Acknowledgments: None

Conflict of Interest: None

Financial Support: None

Ethics Statement: None

References

1. Safarinejad MR, Shafiei N, Safarinejad S. Quality of life and sexual functioning in young women with early-stage breast cancer 1 year after lumpectomy. Psycho-Oncology. 2012;22:1242-48
2. Heemskerk-Gerritsen BAM, Brekelmans CTM, Menke-Pluymers MBE, van Geel AN, Tilanus-Linthorst MMA, Bartels CCM, et al. Prophylactic mastectomy in BRCA1/2 mutation carriers and women at risk of hereditary breast cancer: long-term experiences at the Rotterdam Family Cancer Clinic. Ann Surg Oncol. 2007;14:3335-44
3. Afsharfard A, Mozaffar M, Orang E, Tahmasbpour E. Trends in epidemiology, clinical and histopathological characteristics of breast cancer in Iran: results of a 17 year study. Asian Pac J Cancer Prev. 2013;14:6905-11
4. Yedjou CG, Sims JN, Miele L, Noubissi F, Lowe L, Fonseca DD, et al. Health and racial disparity in breast cancer. Adv Exp Med Biol. 2019;1152:31-49
5. Britt KL, Cuzick J, Phillips KA. Key steps for effective breast cancer prevention. Nat Rev Cancer. 2020;20:417-36
6. Centenera MM, Hickey TE, Jindal S, Ryan NK, Ravindranathan P, Mohammed H, et al. A patient-derived explant (PDE) model of hormone-dependent cancer. Mol Oncol. 2018;12:1608-22
7. Kur P, Kolasa-Wołosiuk A, Misiakiewicz-Has K, Wiszniewska B. Sex hormone-dependent physiology and diseases of liver. Int J Environ Res Public Health. 2020;17:2620
8. Robinson MJ, Cobb MH. Mitogen-activated protein kinase pathways. Curr Opin Cell Biol. 1997;9:180-86
9. Wada T, Penninger JM. Mitogen-activated protein kinases in apoptosis regulation. Oncogene. 2004;23:2838-49
10. Arbabi S, Maier RV. Mitogen-activated protein kinases. Crit Care Med. 2002;30:S74-79
11. Pearson G, Robinson F, Beers Gibson T, Xu BE, Karandikar M, Berman K, et al. Mitogen-activated protein (MAP) kinase pathways: regulation and physiological functions. Endocr Rev. 2001;22:153-83
12. Rose DP, Vona-Davis L. The cellular and molecular mechanisms by which insulin influences breast cancer risk and progression. Endocr Relat Cancer. 2012;19:R225-41
13. He Z, Bateman A. Progranulin (granulin-epithelin precursor, PC-cell-derived growth factor, acrogranin) mediates tissue repair and tumorigenesis. J Mol Med. 2003;81:600-12
14. Yager JD, Davidson NE. Estrogen carcinogenesis in breast cancer. N Engl J Med. 2006;354:270-82
15. Nebert DW, Wikvall K, Miller WL. Human cytochromes P450 in health and disease. Philos Trans R Soc B Biol Sci. 2013;368:20120431
16. Hackett JC. Computational investigations of cytochrome P450 aromatase catalysis and biological evaluation of isoflavone aromatase inhibitors. PhD Thesis, The Ohio State University, Columbus, OH, USA; 2004
17. Lumachi F, Brunello A, Maruzzo M, Basso U, Basso SM. Treatment of estrogen receptor-positive breast cancer. Curr Med Chem. 2013;20:596-604
18. Almeida CF, Oliveira A, Ramos MJ, Fernandes PA, Teixeira N, Amaral C. Estrogen receptor-positive (ER+) breast cancer treatment: are multi-target compounds the next promising approach? Biochem Pharmacol. 2020;177:113989
19. Caciolla J, Bisi A, Belluti F, Rampa A, Gobbi S. Reconsidering aromatase for breast cancer treatment: new roles for an old target. Molecules. 2020;25:5351
20. Patel HK, Bihani T. Selective estrogen receptor modulators (SERMs) and selective estrogen receptor degraders (SERDs) in cancer treatment. Pharmacol Ther. 2018;186:1-24

21. Ratre P, Mishra K, Dubey A, Vyas A, Jain A, Thareja S. Aromatase inhibitors for the treatment of breast cancer: a journey from the scratch. Anti-Cancer Agents Med Chem. 2020;20:1994-2004
22. Ariazi EA, Ariazi JL, Cordera F, Jordan VC. Estrogen receptors as therapeutic targets in breast cancer. Curr Top Med Chem. 2006;6:181-202
23. Grilli S. Tamoxifen (TAM): the dispute goes on. Ann Ist Super Sanita. 2006;42:170
24. Mandlekar S, Kong ANT. Mechanisms of tamoxifen-induced apoptosis. Apoptosis. 2001;6:469-77
25. Rondón-Lagos M, Villegas VE, Rangel N, Sánchez MC, Zaphiropoulos PG. Tamoxifen resistance: emerging molecular targets. Int J Mol Sci. 2016;17:1357
26. Lipsey CC, Harbuzariu A, Daley-Brown D, Gonzalez-Perez RR. Oncogenic role of leptin and Notch interleukin-1 leptin crosstalk outcome in cancer. World J Methodol. 2016;6:43
27. Sukocheva OA, Lukina E, Friedemann M, Menschikowski M, Hagelgans A, Aliev G. The crucial role of epigenetic regulation in breast cancer anti-estrogen resistance: current findings and future perspectives. Semin Cancer Biol. 2020;82:35-59
28. Viedma-Rodríguez R, Baiza-Gutman L, Salamanca-Gómez F, Diaz-Zaragoza M, Martínez-Hernández G, Ruiz Esparza-Garrido R, et al. Mechanisms associated with resistance to tamoxifen in estrogen receptor-positive breast cancer. Oncol Rep. 2014;32:3-15
29. Begam AJ, Jubie S, Nanjan M. Estrogen receptor agonists/antagonists in breast cancer therapy: a critical review. Bioorg Chem. 2017;71:257-74
30. Chin Y, Beresford M, Ravichandran D, Makris A. Exemestane after non-steroidal aromatase inhibitors for post-menopausal women with advanced breast cancer. Breast. 2007;16:436-39
31. Franik S, Eltrop SM, Kremer JA, Kiesel L, Farquhar C. Aromatase inhibitors (letrozole) for subfertile women with polycystic ovary syndrome. Cochrane Database Syst Rev. 2018;2018:CD010287
32. Menu TMSM. Available from: www.rcsb.org (accessed 29 November 2023)
33. Varone A, Amoruso C, Monti M, Patheja M, Greco A, Auletta L, et al. The phosphatase Shp1 interacts with and dephosphorylates cortactin to inhibit invadopodia function. Cell Commun Signal. 2021;19:64
34. Ahlin C, Lundgren C, Embretsén-Varro E, Jirström K, Blomqvist C, Fjällskog ML, et al. High expression of cyclin D1 is associated to high proliferation rate and increased risk of mortality in women with ER-positive but not in ER-negative breast cancers. Breast Cancer Res Treat. 2017;164:667-78
35. Qian S, Wei Z, Yang W, Huang J, Yang Y, Wang J. The role of BCL-2 family proteins in regulating apoptosis and cancer therapy. Front Oncol. 2022;12:985363
36. DeSantis CE, Ma J, Gaudet MM, Newman LA, Miller KD, Goding Sauer A, et al. Breast cancer statistics, 2019. CA Cancer J Clin. 2019;69:438-51
37. Kalluri R, Weinberg RA. The basics of epithelial-mesenchymal transition. J Clin Investig. 2009;119:1420-28
38. Vella V, De Francesco EM, Lappano R, Muoio MG, Manzella L, Maggiolini M, et al. Microenvironmental determinants of breast cancer metastasis: focus on the crucial interplay between estrogen and insulin/insulin-like growth factor signaling. Front Cell Dev Biol. 2020;8:608412
39. Kharb R, Haider K, Neha K, Yar MS. Aromatase inhibitors: role in postmenopausal breast cancer. Arch Der Pharm. 2020;353:e2000081.